

# In Vivo Analysis of Medial Perforant Path-Evoked Excitation and Inhibition in Dentate Granule Cells

 Martin Pofahl,<sup>1</sup>  Daniel Müller-Komorowska,<sup>1</sup>  Jonas Klussmann,<sup>1</sup>  Ilan Lampl,<sup>2</sup>  
and  Heinz Beck<sup>1,3</sup>

<sup>1</sup>Institute of Experimental Epileptology and Cognition Research, University of Bonn, Bonn 53127, Germany, <sup>2</sup>Department of Neurobiology, Weizmann Institute of Science, Rehovot 7610001, Israel, and <sup>3</sup>Deutsches Zentrum für Neurodegenerative Erkrankungen e.V., Bonn 53127, Germany

## Abstract

Across brain regions and species, the dynamics and balance of excitation and inhibition critically determine neuronal firing. The hippocampal dentate gyrus is a brain area thought to be strongly regulated by inhibition. In vivo, it exhibits remarkably sparse activity, a characteristic proposed to underlie computational tasks like pattern separation. Several populations of interneurons mediate strong feedforward as well as feedback inhibition onto granule cells. However, how the dynamics of inhibition controls granule cell activity in vivo is insufficiently studied. Using two-photon in vivo  $\text{Ca}^{2+}$  imaging in mice of either sex, we show that sensory stimulation activates only a small number of dentate gyrus granule cells, while inducing widespread inhibition across the remaining granule cell population. Dual-color imaging of both bulk medial perforant path activity and individual granule cell activity allowed us to probe input–output conversion in this pathway. To examine the interplay of MPP-evoked excitation and inhibition at the cellular level, we used in vivo whole-cell patch-clamp recordings, while simultaneously photo-activating MPP inputs. Our findings reveal that MPP-triggered inhibition is fast, significantly larger than excitation, and long-lasting. These results reveal specific properties of inhibition in the dentate gyrus inhibition that are likely crucial for its computational functions, in maintaining sparse activity with a high signal-to-noise ratio.

**Key words:** dentate gyrus; granule cells; hippocampus; imaging; in vivo patch clamp; inhibition

## Significance Statement

This study investigates the super- and subthreshold computations of dentate gyrus granule cells to an incoming stimulus signal through the medial perforant path the main pathway transferring information from the medial entorhinal cortex layer II into the hippocampus proper. The role of the granule cell network is thought to be crucial for the encoding of new environments and thereby the forming of new memories. Our data directly elucidate the in vivo dynamics of excitation and inhibition in the dentate gyrus using both in vivo imaging and electrophysiology. These findings add to the understanding of the overall sparse code of the dentate gyrus and can be crucial for future studies investigating how hippocampal codes are generated from entorhinal cortex inputs.

## Introduction

The dentate gyrus is a relay structure that conveys multimodal sensory information arriving from the entorhinal cortex to the hippocampus proper. A prevailing concept of dentate gyrus function across species is that it acts as a pattern separator (Leutgeb et al., 2007; Berron et al., 2016; Sakon and Suzuki, 2019), meaning that it is capable of generating dissimilar neuronal representations from similar entorhinal cortex input states (Cayco-Gajic and Silver, 2019). This computational property of the dentate gyrus is

Received Feb. 6, 2025; revised Oct. 23, 2025; accepted Nov. 2, 2025.

The authors declare no competing financial interests.

Author contributions: M.P. and H.B. designed research; M.P. and J.K. performed research; M.P., D.M.-K., and I.L. analyzed data; M.P. and H.B. wrote the paper.

We thank the support of the Imaging Core Facility of the Bonn Technology Campus Life Sciences (Deutsche Forschungsgemeinschaft [DFG], German Research Foundation project no. 266686698). The work was supported by the SFB 1089, Project C04, to H.B., the Research Group FOR2715, the Research Priority Program SPP Computational Connectomics, and EXC 2151 under Germany's Excellence Strategy of the DFG (German Research Foundation) to H.B. We thank N. Nikbakht, F. Distler, N. Masala, P. X. Royero, L. Ewell and H. Oberhaus for fruitful discussions and S. Arnold for patience and support.

*Continued on next page.*

supported by expansion recoding, i.e., a mapping of entorhinal cortex information onto a far larger population of granule cells, but also critically requires granule cell activity to be sparse. This is in good agreement with the sparse range of granule cell activity reported in vivo (Pilz et al., 2016; Hainmueller and Bartos, 2018; Pofahl et al., 2021).

The intrinsic and circuit properties of the dentate gyrus are well suited to support sparse coding. In particular, the dentate gyrus constitutes one of the more heavily inhibited regions of the brain. Numerous in vitro studies have shown that afferent activation via the perforant path recruits remarkably strong and fast feedforward and feedback GABAergic inhibition (Ang et al., 2006; Ewell and Jones, 2010; Li et al., 2013; Espinoza et al., 2018; Mircheva et al., 2019; Braganza et al., 2020). Indeed, inhibition is thought to critically contribute to the function of pattern separation (O'Reilly and McClelland, 1994; Stefanelli et al., 2016; Leal and Yassa, 2018; Madar et al., 2019; Braganza et al., 2020). Furthermore, specific activity patterns of somatostatin versus parvalbumin-expressing interneurons in vivo suggest specific roles of inhibitory subcircuits in encoding novelty (Hainmueller et al., 2024) and predicting goal locations (Yuan et al., 2025). Finally, the dentate gyrus is also critical for forms of spatial memory requiring discrimination of subtle differences (Pofahl et al., 2021). Inhibition appears to also be critical for such forms of memory, with plasticity of interneuron recruitment in feedback circuits as a proposed mechanism (Bartos et al., 2001). However, while these studies shed light on the in vivo recruitment of interneurons in the dentate gyrus, it was still unclear how this is translated to dynamic inhibition of granule cells at the single cell and population levels.

Systematic tracing studies have revealed extensive intrahippocampal connectivity contributing to inhibitory networks (Buckmaster and Schwartzkroin, 1995; Sik et al., 1997; Bienkowski et al., 2018; Yen et al., 2022). Because this long-range excitatory as well as inhibitory connectivity may contribute to dynamic inhibition of granule cells, we used in vivo two-photon imaging and patch-clamp recording approaches to assess how perforant path activation evokes dentate gyrus inhibition and how this inhibition impacts the granule cell ensemble as well as its individual cells.

Our results show that mild aversive sensory stimulation leads to recruitment of a small minority of granule cells, with a long-lasting inhibition of the remaining granule cell population. This sensory input drives transmission through the medial perforant path, with a direct correlation between medial perforant path input and the dentate gyrus output. In vivo whole-cell patch-clamp recordings reveal medial perforant path activation generates inhibition that is fast and four times stronger than excitation. The balance between excitation to inhibition is stable across different stimulus intensities and during repetitive stimulation. These properties likely play a role in ensuring sparse granule cell activity across the physiological spectrum of input frequencies.

## Materials and Methods

**Code availability.** All code manufactured for this study is available under <https://github.com/IEECCR/in-vivo-analysis-of-medial-perforant-path-evoked-excitation-and-inhibition-in-dentate-granule-cells>.

**Data availability.** All data used in this study is available in a dryad repository: <https://doi.org/10.5061/dryad.tdz08kqch>.

**Animals and procedures.** All animal experiments were conducted in accordance with European (2010/63/EU) and federal law (TierSchG, TierSchVersV) on animal care and use and approved by the county of North-Rhine Westphalia (LANUV AZ 84-02.04.2015.A524, AZ 81-02.04.2019.A216). For imaging experiments, we used 9–12-week-old Thy1-GCaMP6 (6 male, 3 female, GP4.12Dkim/J) mice, expressing GCaMP6s in most excitatory hippocampal neurons (Dana et al., 2014). All Thy1-GCaMP6 mice presented in this study were part of a former study where the histology for virus expression was reported (Pofahl et al., 2021). For all patch-clamp experiments, we used male and female wild type C57/BL6 mice.

**Virus injections and head fixation.** Thy1-GCaMP6 mice were anesthetized with a combination of fentanyl/midazolam/medetomidine (0.05/5.0/0.5 mg/kg body weight, i.p.) and head-fixed in a stereotactic frame. Thirty minutes before anesthesia, the animals were

M.P.'s present address: Kavli Institute for Systems Neuroscience and Centre for Algorithms in the Cortex, Norwegian University of Science and Technology, Trondheim 97030, Norway.

Correspondence should be addressed to Martin Pofahl at [martin.pofahl@ntnu.no](mailto:martin.pofahl@ntnu.no).

Copyright © 2025 Pofahl et al. This is an open-access article distributed under the terms of the [Creative Commons Attribution 4.0 International license](https://creativecommons.org/licenses/by/4.0/), which permits unrestricted use, distribution and reproduction in any medium provided that the original work is properly attributed.

given a subcutaneous injection of ketoprofen (5 mg/kg body weight). Eyes were covered with an eye ointment (Bepanthen, Bayer) to prevent drying, and body temperature was maintained at 37°C using a regulated heating plate (TCAT-2LV, Physitemp) and a rectal thermal probe. After removing the head hair and superficial disinfection, the scalp was removed ~1 cm<sup>2</sup> around the middle of the skull. The surface was locally anesthetized with a drop of 10% lidocaine, and after 3–5 min, residual soft tissue was removed from the skull bones with a scraper and 3% H<sub>2</sub>O<sub>2</sub>/NaCl solution. After complete drying, the cranial sutures were clearly visible and served as orientation for determining the drilling and injection sites. For virus injection, a hole was carefully drilled through the skull with a dental drill, avoiding excessive heating and injury to the meninges. Any minor bleeding was stopped with a sterile pad. The target site was located as the joint of parietal, interparietal, and occipital skull plates. Subsequently, the tip of a precision syringe (cannula size 34 G) was navigated stereotactically through the burr hole (30° toward vertical sagittal plane, 1.5 mm depth from skull surface) to target the following coordinates: anteroposterior (AP) measured from bregma ~4.6 mm; lateral (L) specified from midline ~3 mm; dorsoventral (DV) from surface of the skull ~4.2 mm. Virus particles [rAAV2/1-CaMKIIa-NES-jRGECO1a (Dana et al., 2016) or rAAV.CaMKIIa-hChR2(H134R)-mCherry] were slowly injected (total volume 250 nl, 50 nl/min) in the medial entorhinal cortex. Correct injection site in the medial entorhinal cortex was verified by confined expression of jRGECO1a in the middle molecular layer of the dentate gyrus. To prevent reflux of the injected fluid, the cannula was retained for 5 min at the injection site. For mice used for patching experiments, the skin was sealed using surgical suture. For mice used for imaging, OptiBond (OptiBond 3FL; two-component, 48% filled dental adhesive, bottle kit; Kerr) was applied thinly to the skull to aid adhesion of dental cement. Subsequently, a flat custom-made head post ring was applied with the aid of dental cement (Tetric EvoFlow), the borehole was closed and the surrounding skin adapted with tissue glue. At the end of the surgery, anesthesia was terminated by intraperitoneal injection of antagonists (naloxone/flumazenil/atipamezole, 1.2/0.5/2.5 mg/kg body weight). Postoperative analgesia was carried out over 3 d with once daily ketoprofen (5 mg/kg body weight, s.c.).

**Window implantation procedure.** Cranial window surgery was performed to allow imaging of the hippocampal dentate gyrus. Thirty minutes before the induction of anesthesia, the analgesic buprenorphine was administered for analgesia (0.05 mg/kg body weight) and dexamethasone (0.1 mg/20 g body weight) was given to inhibit inflammation. Mice were anesthetized with 3–4% isoflurane in an oxygen/air mixture (25/75%) and then placed in a stereotactic frame. Eyes were covered with an eye ointment (Bepanthen, Bayer) to prevent drying and body temperature was maintained at 37°C using a regulated heating plate (TCAT-2LV, Physitemp) and a rectal thermal probe. The further anesthesia was carried out via a mask with a reduced isoflurane dose of 1–2% at a gas flow of ~0.5 L/min. A circular craniotomy (Ø, 3 mm) was opened above the right hemisphere hippocampus using a dental drill. Cortical and CA1 tissue was aspirated using a blunted 27-gauge needle until the blood vessels above the dentate gyrus became visible. Even though the aspirated volume was kept to an absolute minimum, we cannot exclude that this type of window surgery might lead to altered dentate gyrus activity. For instance, interneurons projecting from CA1 to dentate gyrus have been described that might normally modulate granule cell activity (Szabo et al., 2017). A custom-made cone-shaped silicon inset (upper diameter, 3 mm; lower diameter, 1.5 mm; length, 2.3 mm; RTV 615, Momentive) attached to by a cover glass (Ø, 5 mm; thickness, 0.17 mm) was inserted and fixed with dental cement. Postoperative care included analgesia by administering buprenorphine twice daily (0.05 mg/kg body weight) and ketoprofen once daily (5 mg/kg body weight, s.c.) on 3 consecutive days after surgery. Animals were carefully monitored twice daily on the following 3 d and recovered from surgery within 24–48 h, showing normal activity and no signs of pain.

**Two-photon calcium imaging.** We used a commercially available two-photon microscope (A1 MP, Nikon) equipped with a 25× long-working-distance, water-immersion objective (NA = 1, WD = 4 mm, XLPLN25XSVM2, Olympus) controlled by NIS-Elements software (Nikon). GCaMP6s was excited at 940 nm using a Ti:Sapphire laser system (~60 fs laser pulse width; Chameleon Vision-S, Coherent) and a fiber laser system at 1,070 nm (55 fs laser pulse width, Fidelity-2, Coherent) to excite jRGECO1a. Emitted photons were collected using gated GaAsP photomultipliers (H11706-40, Hamamatsu). Movies were recorded using a resonant scanning system at a frame rate of 15 Hz and duration of 20 min per movie.

**Habituation and behavior on the linear track.** Imaging experiments were performed in head-fixed awake mice running on a treadmill. Two weeks before the measurements, mice were habituated to the head fixation. Initially mice were placed on the treadmill without fixation for 5 min at a time. Subsequently, mice were head-fixed, but immediately removed if signs of fear or anxiety were observed. These habituation sessions lasted 5 min each and were carried out three times per day, flanked by 5 min of handling. During the following 3–5 d, sessions were extended to 10 min each. The duration of sessions used for experiments was 20 min each.

**Air puff stimulation.** During a recording between 36 and 77 air puff stimuli were presented (58 ± 5 stimulations per mouse) on the animals back. The air flow was controlled by a solenoid valve with a pressure of 1 Bar before the valve. The air outlet was a 1 ml pipette tip (Thermo Fisher Scientific). The duration of each air puff was 250 ms. Stimulation only happened when the animal was at rest. The mean probability of delivering an air puff at any given second during

resting periods was 0.06. Time intervals between stopping of the animal and the first air puff and interstimulation intervals were randomized (1–50 s) and were applied at random positions on the linear track to prevent the animal from anticipating the stimulation.

*Pupil diameter measurement and analysis.* On the linear track, the pupil diameter was measured using a high-speed camera (Basler Pilot, Basler) at a framerate of 100 Hz. To estimate pupil diameter, a circular shape was fitted to the pupil using the LabView NI Vision toolbox (National Instruments), providing a real-time readout. Post hoc, the pupil diameter trace was normalized to its mean. As in a published study (Reimer et al., 2014), frames in which pupil diameters could not be obtained due to blinking or saccades were removed from the trace. The pupil diameter trace was filtered using a Butterworth low-pass filter at a cutoff frequency of 4 Hz. To match the time resolution of the imaging data, the pupil trace was downsampled to 15 Hz. To test whether the pupil constriction after air puffs could serve a classifier for the stimulus, we used ROC analysis. ROC curves were computed by comparing the normalized pupil size in a 1 s time windows pre-versus poststimuli. A series of thresholds was set from the minimum to the maximum number of pupil sizes recorded in each mouse. For each threshold, we calculated the probability that the pupil size was below the threshold in the prestimulus window and in the poststimulus window that defined the false positive rate and the true positive rate, respectively. The ROC curve is produced by plotting the true positive rate against the false positive rate, and the area under the curve (AUC) defines the responsiveness of each cell. To test the significance of responsiveness, we produced shuffled distributions by randomly shuffling the pre- and poststimulus values 1,000 times. For all mice the pupil response resulted in an AUC > 0.7 and above a 95th percentile of its shuffled distribution.

*Individual response analysis and data shuffling.* To estimate significant responses of each neuronal or behavioral read-out variable for each applied air puff stimulus, we compared the variable with the variance of its baseline and a shuffled distribution. The shuffled distributions were generated by randomly reassigning the times of stimulation to other times when the animal was at rest. Actual stimulation time points were excluded, and every new time point  $\pm 1$  s could be picked only once. The shuffled data was read out from the shuffled time points, and this procedure was repeated 100 times. The shuffled baseline with 95th percentile for each variable was calculated from the accumulated shuffled data. For each variable, the comparison to its baseline was as follows: The onset of locomotion was considered significant if the speed of the animal exceeded a threshold of 4 cm/s after the stimulus. The pupil response was considered significant if the pupil size after the stimulus exceeded two standard deviations of its size window before the stimulus. The response of a granule cell ensemble was considered significant if the event rate exceeded two standard deviations of its baseline after stimulus. The response of the MPP activity was considered significant for individual stimuli if the Df/F signal after stimulus exceed 2 standard deviations of its baseline.

*Data analysis: two-photon imaging.* All analysis on imaging data and treadmill behavior data were conducted in MATLAB using standard toolboxes, open access toolboxes, and custom-written code. To remove motion artifacts, recorded movies were registered using a Lucas–Kanade model (Greenberg and Kerr, 2009). Air puff stimulation or the induced behavioral responses did not induce movement artifacts that were stronger than usual movement artifacts in head fixed imaging data. Individual cell locations and fluorescence traces were identified using a constrained non-negative matrix factorization-based algorithm, and afterward  $\text{Ca}^{2+}$  events were identified with a constrained deconvolution algorithm (Pnevmatikakis et al., 2016). The algorithm is dependent on fluorescence changes to identify components and is biased toward active cells. We therefore restricted all analysis to active cells that showed least one  $\text{Ca}^{2+}$  event with an amplitude 3 standard deviations above noise level in their extracted fluorescence trace. All components were manually inspected and only those that showed shape and size of a granule cell were kept. We binarized individual cell fluorescence traces by converting the onsets of detected  $\text{Ca}^{2+}$  events to binary activity events. We did not observe any indication of epileptiform activity in Thy1-GCaMP6 (GP4.12Dkim/J) mice, in line with previous work (Steinmetz et al., 2017).

*Analysis of MPP input signals.* MPP input bulk signal was analyzed by setting a region of interest in the molecular layer. For that, a threshold of 50% maximum fluorescence was used within the field of view on the average projection of the movie. The bulk fluorescence signal trace was calculated as the average signal of the defined region of interest in each frame. The baseline for the bulk signal was defined as the low-pass filtered signal of the raw trace with a cutoff frequency of 0.01 Hz using a Butterworth filter model. We used a constrained deconvolution algorithm (Pnevmatikakis et al., 2016) to create a proxy for the underlying activity of the bulk signal. This allowed for identification of precise onset times and normalized amplitude values of  $\text{Ca}^{2+}$  events in MPP input data. To test whether the MPP signal after air puffs could serve a classifier for the stimulus, we used ROC analysis. ROC curves were computed by comparing the normalized Df/F signal in a 1 s time windows pre- versus poststimuli. A series of thresholds was set from the minimum to the maximum number of values recorded in each mouse. For each threshold, we calculated the probability that the Df/F value was below the threshold. For the prestimulus window that defined the false positive rate and for the post stimulus window that defined the true positive rate. The ROC curve is produced by plotting the true positive rate against the false positive rate, and the area under the curve (AUC) defines the responsiveness of the signal. To test the significance of responsiveness, we produced

shuffled distributions by randomly shuffling the pre- and poststimulus values 1,000 times. For all mice, the MPP signal resulted in an AUC > 0.85 and above a 95th percentile of its shuffled distribution.

*Air puff responding cells and ROC analysis.* To test whether individual granule cell significantly respond to air puffs, we used ROC analysis (Liu et al., 2025). ROC curves were computed by comparing the number of significant calcium transient onsets in a 1 s time windows pre- versus poststimuli. A series of thresholds was set from the minimum to the maximum number of onsets recorded for each granule cell. For each threshold, we calculated the probability that the event value was below the threshold in the prestimulus window and in the poststimulus window that defined the false positive rate and the true positive rate, respectively. The ROC curve is produced by plotting the true positive rate against the false positive rate, and the area under the curve (AUC) defines the responsiveness of the signal. To test the significance of responsiveness, we produced shuffled distributions by randomly shuffling the pre- and poststimulus values 1,000 times. A granule cells was termed a responder if it showed AUC > 0.5 and above a 95th percentile of its shuffled distribution. For the ensemble signals, we used the same approach calculating the sets of thresholds from the averaged and z-scored data.

*Fitting response dynamics.* To analyze the time courses of the response dynamics, we fitted an exponential rise combined with an exponential decay onto the averaged event probabilities of the responding as well as the nonresponding granule cells. The dynamic function had the following form:

$$f_{\text{dyn}}(t) = A(1 - \exp(-t/\tau_{\text{fall}})) \exp(-t/\tau_{\text{rise}}) + C,$$

where  $A$  is the amplitude of the function,  $\tau_{\text{rise}}$  is the time constant for the exponential rise,  $\tau_{\text{fall}}$  is the time constant of the exponential decay, and  $C$  is a constant resembling the baseline event probability. For fitting we used the `fminsearch` MATLAB routine. To estimate the 95% confidence intervals, we used a bootstrapping approach in which we randomly shuffled each data point within its SEM range and repeated the fit to the shuffled data. We repeated this procedure 1,000 times to determine the distributions for the fitted parameters from which we took the 95% confidence intervals. Since the data can be fitted with a wider range of combinations of  $A$ ,  $\tau_{\text{rise}}$ , and  $\tau_{\text{fall}}$ , we used the FWHM as a readout to determine the duration of the dynamics.

*Linear mixed model.* To test amplitude differences of granule cell ensembles in different behavioral conditions while considering repeated measures and individual mouse contributions, we fitted linear mixed models to the poststimulus amplitudes using the `fitlme` MATLAB routine. The fitted model was as follows:

$$\text{response} \sim \text{condition} + (1 | \text{animal}) + (1 | \text{animal:neuron}),$$

where `response` is the response amplitudes of granule cells, `condition` is the behavioral condition (air puff with running onset, air puff without running onset, all air puff stimulation, or spontaneous running onset), `animal` refers to the individual mouse, and `animal:neuron` refers to the cells nested within individual mice. To test for significance without assuming normally distributed data, we calculated the rank of each cell response and performed a permutation test with 1,000 iterations.

*Correlation analysis.* Cross-correlations were calculated using the `xcorr` MATLAB routine on the average Df/F traces across stimuli of MPP bulk signal and mean granule cell signal. For individual correlations, we used the averaged MPP bulk signal and the individual granule cell signal averaged across trials. The Pearson's correlation coefficient of these traces was calculated for quantification. For noise correlations, the mean response of each individual cell was subtracted from the individual response of that cell. The same was done for the MPP input trace. The noise correlation was calculated as the Pearson's correlation using the peak values of these traces across trials.

*In vivo patch-clamp experiments.* Three weeks after virus injection, mice were anesthetized with ketamin (0.1 ml ketamin, 0.075 ml xylazine, 0.225 ml Saline) and the analgesic buprenorphine was administered for analgesia (0.05 mg/kg body weight). Eyes were covered with an eye ointment (Bepanthen, Bayer) to prevent drying and body temperature was maintained at 37°C using a regulated heating plate (TCAT-2LV, Physitemp) and a rectal thermal probe. After removal of the head hair and superficial disinfection, the scalp was removed ~1 cm<sup>2</sup> around the middle of the skull. The surface was locally anesthetized with a drop of 10% lidocaine, and after 3–5 min residual soft tissue was removed from the skull bones with a scraper and 3% H<sub>2</sub>O<sub>2</sub>/NaCl solution. After complete drying, the cranial sutures were clearly visible and served as orientation for the determination of the drilling and injection sites. A custom-made headpost was fixed on the skull using UV curing glue (4305, Loctite) and the animal was head fixed. A tube was inserted into the animal's trachea to control breathing, monitor oxygen level, and induce the anesthesia with 1–2% isoflurane throughout the experiment. A multimode light fiber was implanted into MEC through the craniotomy that was drilled during virus injection under an angle of 15° with respect to the anteroposterior axis. Above the hippocampus the skull was carefully opened using a dental drill. The dura

was carefully removed without injuring the underlying cortex tissue. The blind patching followed a formerly described protocol (Okun and Lampl, 2008; Cohen-Kashi Malina et al., 2016). Briefly, a patch pipette was vertically inserted into the cortex and carefully lowered to the depth of the DG granule cell layer. The intracellular solution for current-clamp experiments contained the following (in mM): 136 K-gluconate, 5 NaCl, 10 KCl, 10 HEPES, 1 MgATP, 0.3 NaGTP, 10 phosphocreatine, 2 QX314, biocytin. The approach to a putative granule cell was identified monitoring resistance response at the pipette tip. After successful giga-seal and cell opening, the cell was measured in current clamp. For a unique identification of cells, only one cell per session was measured. During experiments MEC cell somata were stimulated with 473 nm light administered from a diode laser through the implanted light fiber.

Inhibitory and excitatory conductance were calculated following a formerly described procedure (Priebe and Ferster, 2005). Briefly, a simplified membrane equation was utilized:

$$I_{inj} = C \frac{dV}{dt} + G_r(V_t - E_r) + G_e(V_t - V_e) + G_i(V_t - V_i),$$

where  $I_{inj}$  is the clamped current,  $C$  is the membrane capacitance,  $V$  is the measured voltage,  $G_r$  is the leak conductance,  $E_r$  is the resting potential, and  $V_e$  and  $V_i$  are the summarized reversal potentials for all excitatory and inhibitory channels, respectively.  $G_e$  and  $G_i$  are the excitatory and inhibitory conductance, respectively. The resting membrane potential was measured in resting condition of the cell. The reversal potentials were assumed as constant and were defined by the in-solution composition. The leak conductance  $G_r$  was estimated using the voltage step size after current injection at steady state:

$$G_r = \Delta I / \Delta V,$$

where the final conductance was taken as the average of all current voltage combinations during one measurement. The membrane capacitance  $C$  was estimated by fitting time course of the membrane charging after current injection and estimating the charging time constant  $\tau$ . The capacitance is then given by the following:

$$C = \tau G_r.$$

To correct for nonideal patching conditions the constants were further fitted by injecting different current values so that the resulting passive properties of the cell were matched. Conductances were measured by measuring the voltage response to MPP stimulation at four different clamped current values. Each measurement delivered a linear solution for the conductances, so in total four linear solutions. The final values for both conductances were set as the center of mass of all intersections of all four solutions. To test the found solutions, theoretical voltage traces were reconstructed that used the estimated values for the conductances. To estimate the goodness of fit, the mean squared error, the  $R^2$  value, and the Pearson's correlation between the input voltage traces and the reconstructed traces were calculated for time windows of 1 s after each stimulus.

Post hoc, the biocytin filled cell was stained with streptavidin 488 and recovered in fixed tissue. Cell nuclei were stained with DAPI allowing the identification of the granule cell layer. A measured cell was included only if it was found within the granule cell layer and morphologically identified as granule cell (21/35 of patched cells). Experiments were included only if viral expression could be confirmed within the medial molecular layer of DG (9/21 of successful patching sessions).

*In vitro patch-clamp experiments.* Isoflurane anesthesia was used to rapidly decapitate adult male and female mice 10–14 weeks old expressing ChR2 in the MEC (see viral injection procedures). Dissected brains were transferred to carbonated artificial cerebrospinal fluid (ACSF) with sucrose (ice cold; in mM: 60 NaCl, 100 sucrose, 2.5 KCL, 1.25 NaH<sub>2</sub>PO<sub>4</sub>, 26 NaHCO<sub>3</sub>, 1 CaCl<sub>2</sub>, 5 MgCl<sub>2</sub>, 20 glucose; from Sigma-Aldrich). Then, 300- $\mu$ m-thick coronal slices were transferred to the same ACSF with sucrose at 37°C for 20 min. Slices were then kept and sliced in ACSF without sucrose (in mM: 125 NaCl, 3.5 KCL, 1.25 104 NaH<sub>2</sub>PO<sub>4</sub>, 26 NaHCO<sub>3</sub>, 2 CaCl<sub>2</sub>, 2 MgCl<sub>2</sub>, 20 glucose; from Sigma-Aldrich). The intracellular solution for voltage-clamp experiments contained the following (in mM): 120 Cs methanesulfonate, 0.5 MgCl<sub>2</sub>, 5 2-(4-(2-hydroxyethyl)-1-piperazinyl)-ethansulfonsäure (HEPES), 5 ethyleneglycol-bis(aminoethylether)-*N,N,N',N'*-tetraacetic acid (EGTA), 5 adenosine 5'-triphosphate disodium salt (Na<sub>2</sub>-ATP), 5 *N*-(2,6-dimethylphenylcarbamoylmethyl)triethylammonium chloride (QX 314 Cl<sup>-</sup>); from Sigma-Aldrich. Granule cells were patched at room temperature central in the upper blade of dorsal dentate gyrus, to target mature granule cells comparable to those targeted in the *in vivo* patching and imaging experiments. To isolate monosynaptic responses, we used ACSF with 1  $\mu$ M tetrodotoxin (TTX, Tocris), 200  $\mu$ M 4-aminopyridine (4-AP, 112 Sigma-Aldrich). To isolate excitatory conductances, we used 10  $\mu$ M gabazine (SR 95531 hydrobromide; Tocris). Patch-clamp experiments were performed with a MultiClamp 700B and digitized on an Axon Digidata 1550A. Light stimulation was performed with an Omicron LuxX 473 nm laser attached to a light fiber submerged in the ACSF. Light stimuli were 10 ms long. To isolate excitatory and inhibitory conductances, we assumed a chloride reversal of -80 mV and a cation reversal potential of 0 mV. Furthermore, we used gabazine to isolate the excitatory conductance. The excitatory

conductance we report was calculated with gabazine washed in at a corrected holding potential (liquid junction potential:  $-9$  mV) of  $-80$  mV. The inhibitory conductance we report was calculated at a corrected holding potential of  $0$  mV and subtracting the response recorded with gabazine from the baseline response under ACSF. Recordings were performed at room temperature.

## Results

### Sensory stimulation leads to an activation of a small subset of granule cells and widespread inhibition of the remaining population

We imaged the activity of 1,583 active granule cells [ $176 \pm 57$  active cells per field of view (FOV)] in nine mice expressing GCaMP6s under the Thy1 promoter (GP4.12Dkim/J; Dana et al., 2014; Extended Data Fig. 1-1A). Two-photon imaging in head-fixed mice was carried out while the mice ran on a linear track (Fig. 1A,B). To prevent confounding factors of landmarks or spatially defined food rewards, the mice ran in darkness without any reward on a running belt that was cue enriched but without separate zones or distinct landmarks. We used a constrained nonnegative matrix factorization-based algorithm to identify active granule cells in each FOV (Pnevmatikakis et al., 2016). All analysis in this study is restricted to active granule cells and the onsets of significant  $\text{Ca}^{2+}$  transients are used as a readout of cell activity. To examine the activity responses of granule cells to a physiological input signal, we used a mild air puff administered to the back, since air puff stimulation has been shown to cause reliable activation of hippocampal neurons (Barth et al., 2023). Because the activity profile of dentate granule cells in head-fixed mice can vary significantly with locomotor state, we restricted all stimulation times to periods of immobility (Fig. 1C; Danielson et al., 2016; Pofahl et al., 2021). During a 20-min-long session 36–77 air puff stimuli were presented (Extended Data Fig. 1-1B, 519 stimulations in total,  $58 \pm 5$  stimulations per mouse). To prevent the animal from anticipating the stimulation, time intervals between stopping of the animal and the first air puff and inter-stimulation intervals were randomized (1–50 s; Extended Data Fig. 1-1C,D) and were applied at random positions on the linear track. We used pupil dynamics as a readout of successful stimulation since air puffs can trigger responses in pupil size (Fig. 1D). ROC analysis revealed that rapid pupil constrictions following the stimulus can serve a classifier for air puff stimulation which was significant for every individual mouse (Fig. 1E). To define a successful stimulation, we checked whether the pupil constriction in each individual trial exceeded a 2-sigma threshold compared with baseline, which was the case in  $92 \pm 2\%$  of all stimulus presentations and reliable across mice (Fig. 1D, Extended Data Fig. 1-1E,  $n = 519$  stimuli). For trials without pupil constriction, we found indeed less evidence of the responses we found in later parts of this study (Extended Data Fig. 1-1F–I). The observed rapid pupil constrictions are distinct from slower pupil dilations observed after changes in locomotor state (Pofahl et al., 2021).

We first asked if there is an observable neuronal response to the air puff stimulation in dentate gyrus. Granule cells show generally low activity levels, which can individually vary over a wide range (Pilz et al., 2016; Hainmueller and Bartos, 2018; Pofahl et al., 2021). Indeed, we found the activity of granule cells around the air puff stimulation to be very sparse (Fig. 1F,G). We therefore first quantified how many granule cells had at least a single detected calcium transient onset in a 1-s-long response window after a given air puff (Fig. 1H). In line with the generally sparse activity, this analysis showed that on average 2% of granule cells were active following each air puff. Further, we found that 23% of air puffs were not followed by any granule cell activation and that no air puff was followed by  $>10\%$  active cells of the imaged granule cell population. The comparison to a shuffled distribution showed that the mean recruitment of granule cells following the air puff was even less than the average number of active cells during other moments of immobility (Fig. 1H, gray line, permutation test of mean,  $p = 0.003$ ). Next, we asked how reliably those granule cells that were active following the stimulus were activated. We found that 32% of granule cells were active following a stimulus at least once and 18% were active exactly once (Fig. 1I). However, this distribution had a long tail saturating at 67% of responded stimuli. This suggested that there is a small subset of granule cells that is more reliably triggered by the air puff stimulation.

To test whether individual granule cells significantly respond to air puffs, we used ROC analysis (Liu et al., 2025) to compare the activity of individual granule cells after the stimulation to the baseline activity. If this difference could classify the occurrence of an air puff with an area under the curve (AUC)  $> 0.5$  and above a 95th percentile chance level, the granule cell was considered a significant responder (Extended Data Fig. 1-1J and Materials and Methods). Using this quantitative responder definition (Fig. 1J,K), we found in total 38/1,583 responders (Fig. 1L), corresponding to  $2.6 \pm 0.6\%$  of granule cells across mice (Extended Data Fig. 1-1K,L). We termed the significantly responding granule cells AP+ cells and summarized all other granule cells as AP– cells. Within the AP+ set, half of the cells responded to  $<25\%$  of stimuli, with a small group of cells responding to  $\sim 50\%$  of the stimuli (Fig. 1M,  $n = 38$  cells from 9 mice). This demonstrates that even in AP+ cell set, responses are quite unreliable across stimulations. These differences in air puff responsiveness are correlated to the overall cell activity during a recording (Extended Data Fig. 1-1M,  $r = 0.66$ ,  $p < 0.001$ ,  $n = 38$  cells), suggesting that an overall excitability determines how reliable a cell can follow incoming stimuli. Of note, the exact definition of the AP+ granule cells did not change any of the results, as five different definitions of responders were tried for the analysis which all led to a high overlap of identified cells and comparable results (Extended Data Fig. 1-2). The ROC analysis was chosen since it was the most conservative definition and contained only cells that were also identified by other definitions (Extended Data Fig. 1-2A,B).

Consistent with the sparse air puff responses, quantifying the responses to a given air puff averaging all granule cells across mice did not show a clear peak following any air puff stimulation (Fig. 1N, top panel). Accordingly, the grand



average of this signal was within the 95th percentile of the shuffled signal (Fig. 1N, bottom panel). When restricting this analysis only to the AP+ cells, we expectedly identified a clear peak after the air puffs (Fig. 1O, top panel) also clearly visible in the grand average (Fig. 1O, bottom panel). We then looked at the activity of the complementary AP- cells. Even though the baseline levels of activity in these granule cells were low, the averaged event rates of these cells dropped even further after air puff stimulation (Fig. 1P, top panel). This was reflected in a significant drop of activity after air puff stimulation compared with a shuffled distribution (Fig. 1P, bottom panel,  $n = 1,545$  cells). These results suggest a widespread inhibition of the AP- cell set, triggered by the air puff stimulation.

To analyze whether the ensemble signal in any of these group definitions could serve as a classifier for the air puff stimuli, we performed ROC analysis on the average signals (Fig. 1Q). The AUC derived from average signal from all granule cells was  $\sim 0.5$  in all animals and could not decode the air puff times better than shuffled data (Fig. 1Q; individual mice in Extended Data Fig. 1-1M). The AP+ cells could decode the air puff times in all mice better than the shuffled data (Fig. 1Q; individual mice in Extended Data Fig. 1-1O). Still, the AUC was close to 0.5 in some animals that had a small number of significant responders. Overall, the performance of this analysis was correlated to the absolute number of identified AP+ cells (Extended Data Fig. 1-1Q) but not to differences in the relative number of responders (Extended Data Fig. 1-1R). For the AP- cells, we found AUCs significantly lower than 0.5 in 8/9 animals (Extended Data Fig. 1-1P) and a similar phenomenon in the average of all mice (Fig. 1Q). Statistical analysis showed that AP+ cells had a significantly higher AUC, while the AP- cells had a significantly lower AUC compared with all granule cells [Fig. 1R; repeated-measures ANOVA ( $n = 9$ ,  $F = 22$ ,  $p < 0.001$ ), Bonferroni's correction for pairwise comparisons all  $p < 0.01$ ]. This shows that decoding of the air puff is not possible with the average activity of all granule cells, but the presence of an air puff can be classified using only the responding AP+ cell population, as well as to a lesser extent the complementary AP- cell population.

### Excitation and inhibition of granule cells follow different time courses

Next, we asked if the time courses of the excitation and the inhibition of granule cells following the air puff stimulation differ from each other. To this end, we analyzed the activity of individual granule cells averaged over all stimulations. AP- granule cells not belonging to the responder group showed a slight but visible decrease of activity (150 randomly drawn examples in Fig. 2A). The significantly responding AP+ cells, on the other hand, showed clear and sharper responses (Fig. 2B). We analyzed time course of the responses by fitting the averaged responses of each individual cell with a double exponential function (see Materials and Methods). We found that some responses were sharp, while others seem to maintain an elevated activity level after their response onset (Fig. 2B,C). We also found that the response onsets after stimuli varied across cells (Fig. 2C,D). While  $\sim 50\%$  of granule cells respond faster than 150 ms (corresponding to two frames in our recording), we found that onset delays can be as late as 500 ms.

Given these differences in response dynamics, we wondered if the activity of individual granule cells or the cell ensemble is influenced by the onset of locomotion since the input-output dynamics of the dentate differ between locomotion and rest (Pofahl et al., 2021). Therefore, we subdivided the stimulation episodes into those which were associated with no

←

represents shuffled data with 95th percentiles. **D**, Pupil constriction after air puff stimulation (yellow line with SEM). Pupil diameter averaged over all stimuli and mice ( $n = 519$  stimuli in 9 mice). The gray line represents shuffled data with 95th percentiles. Extended Data Figure 1-1E shows the percentage of significant pupil constrictions for each animal. Extended Data Figure 1-1F-I shows neuronal and behavioral readouts for stimuli that did not cause significant pupil constriction. **E**, ROC analysis for the pupil constriction following air puff stimulation. Gray lines represent the response curves from individual animals; yellow line represents the response curve of the pooled data ( $n = 9$  mice). **F, G**, Examples activity profiles of two granule cells around the air puff stimulation. Top panels: Denoised  $\text{Ca}^{2+}$  activity (gray traces) aligned to stimulus times (red bars). Middle panels, Raster plots of the  $\text{Ca}^{2+}$  event onsets after individual air puff stimulations. Bottom panels, Heat map reflecting the average of  $\text{Ca}^{2+}$  event onsets. **H**, Histogram showing the number of activated granule cells per air puff (gray bars). The blue line represents the cumulative distribution of the same data. The gray line represents the distribution of shuffled data with 95th percentile. The mean of responses after air puffs is significantly lower than for the shuffled data (permutation test,  $n = 1,000$  iterations,  $p = 0.003$ ). **I**, Histogram showing the number of responded air puffs per granule cell (gray bars) for all granule cells that were active at least once following an air puff. The blue line represents the cumulative distribution of the same data. **J, K**, Examples of two air puff responding granule cells. Top panels, Denoised  $\text{Ca}^{2+}$  activity (gray traces) aligned to stimulus times (red bars). Middle panels, Raster plots of the  $\text{Ca}^{2+}$  event onsets after individual air puff stimulations. Bottom panels, Heat map reflecting the average of  $\text{Ca}^{2+}$  event onsets. Extended Data Figure 1-1J shows the ROC curves for individual granule cells. **L**, Fraction of significantly responding granule cells (2.6%, dark blue), nonsignificantly responding granule cells (29.9%, light blue) and never responding granule cells (67.5%, gray) of all granule cells in the dataset. Extended Data Figure 1-1K,L shows number and percentage of significant responding granule cells per animal. **M**, Histogram showing the number of responded air puffs per granule cell (gray bars) for significantly responding granule cells. The blue line represents the cumulative distribution of the same data. **N**, Top panel, Averaged activity of all granule cells in a 4 s window around every air puff across session ( $n = 1,583$  cells from 9 mice). Event onsets per frame were averaged over cells and then z-scored. To match different numbers of stimuli, the responses were resampled to 50 stimuli. The color bar indicates the sigma values of the z-scored signal. The red line denotes the time of the air puff presentation. Bottom panel, Z-scored  $\text{Ca}^{2+}$  event onset probability of all granule cells (black line with SEM). Data is averaged over all cells and stimuli and z-scored with respect to baseline. The gray line represents shuffled data with 95th percentiles. **O**, Same as **N** but only for significantly responding AP+ granule cells ( $n = 38$  cells from 9 mice). **P**, Same as **N** for the AP- cells (all granule cells except the significantly responding ones,  $n = 1,545$  cells from 9 mice). **Q**, ROC analysis curves for the mean signals of all granule cells. For all cells (black line) the difference to 0.5 is not significant. For AP+ cells (dark blue line), the AUC is closer to 1 and significant against shuffle. For the AP- cells (light blue line), the curve is slightly less than 0.5 and significant against shuffle. Extended Data Figure 1-1N-P shows the ROC curves for individual animals. **R**, Comparison of AUC for all granule cells (black), AP+ cells (dark blue) and AP- cells (light blue) for different mice. Gray lines denote individual animals. Repeated-measures ANOVA ( $n = 9$  mice,  $F = 22$ ,  $p < 0.001$ ), Bonferroni's correction for pairwise comparisons all  $p < 0.01$ ). Extended Data Figure 1-2 shows the comparison for different responder definitions. Panels **L**, **O**, **P**, and **Q** are reproduced for these different definitions.

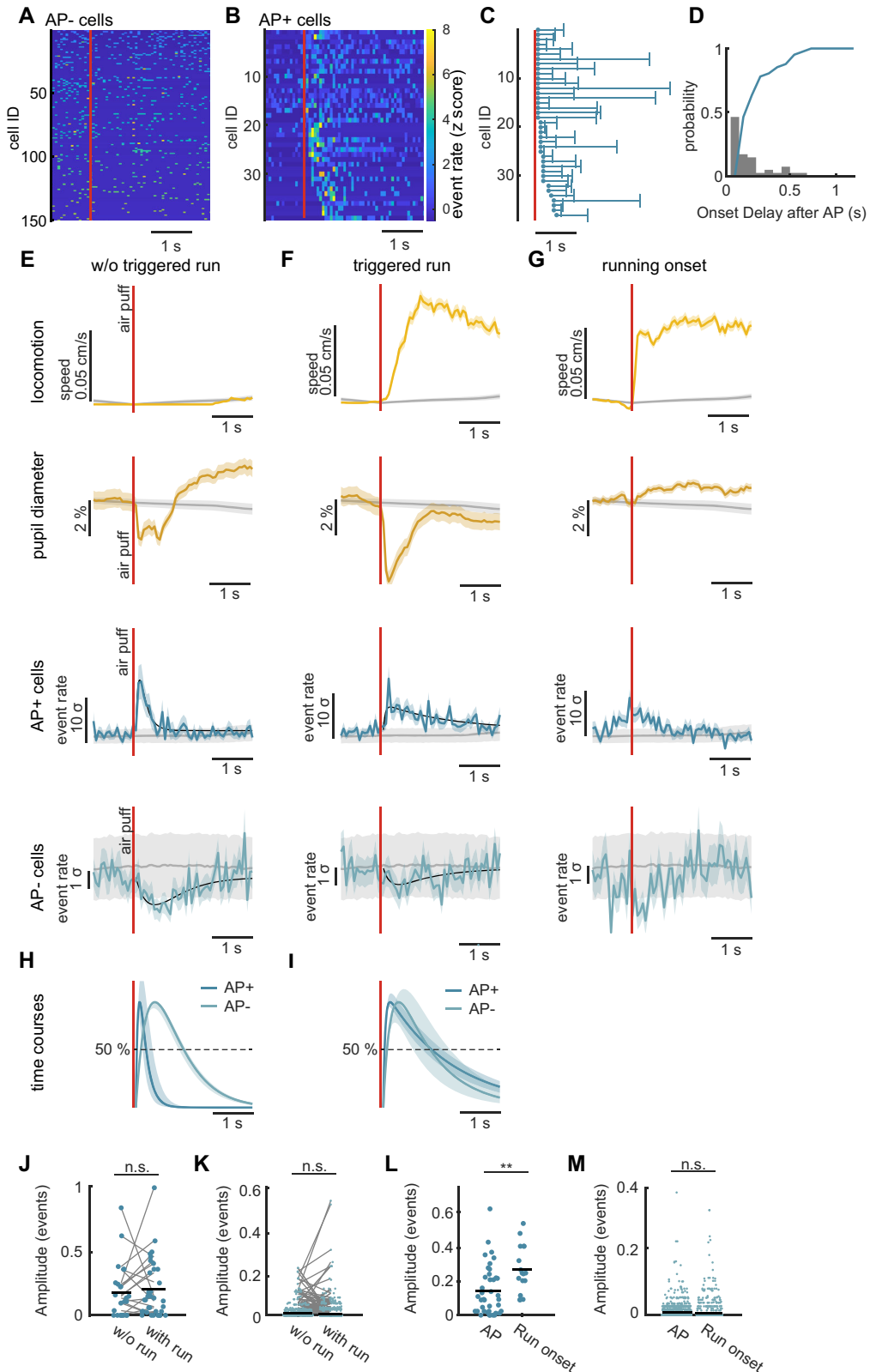


**Figure 2.** Time course of activation versus inhibition of granule cells. **A**, Z-scored heatmaps of 150 nonresponding AP- granule cells from one example mouse. Color bar similar to panel **B** for z-score values. **B**, Z-scored heatmaps of all air puff responding AP+ granule cells of all mice ( $n = 38$  cells from 9 mice). Color bar denoting the z-score value. **C**, Time courses of AP+ cells shown in **B**. Points represent the response onset of each cell and the whisker the FWHM of the activation of the respective cell. **D**, Histogram showing the number of AP+ cells with a specific response onset delay (gray bars). The blue line represents the cumulative distribution of the same data. **E**, For air puffs without triggered running onset: Top yellow panel, Mean running speed after

running response (Fig. 2E, air puff without triggered run) and those that triggered a running onset (Fig. 2F, air puff with triggered run). Air puff stimuli triggered running onsets in  $48 \pm 9\%$  of stimulations. At the same time  $55 \pm 10\%$  of air puffs led to a significant response in the ensemble signal of AP+ granule cells, where a significant response was defined as an amplitude of two sigma above the baseline level. There was no systematic correlation between triggered running onsets and significant responses of the AP+ ensemble signal (Extended Data Fig. 2-1A). For individual AP+ cells, we found that some cells seemed to respond preferentially in scenarios with or without a running onset but did not observe a general trend for one preference (Extended Data Fig. 2-1B-E). We observed differences in pupil diameter between conditions, at later stages  $>1$  s after the air puff stimulation. This can be explained by a general correlation between running speed and pupil expansion leading to more dilated pupils at rest than during locomotion (Fig. 2G; Pofahl et al., 2021).

We then looked systematically at the activity of the AP+ and AP- groups in response to stimulation with and without locomotion onsets. For stimuli without triggered running initiation, AP+ cells show a sharp positive response, while AP- cells displayed an average reduction of activity, as previously observed for the mean of all air puff stimulations (Fig. 2E). For the air puffs that triggered running onsets, we found slowly decaying responses in the AP+ cells (Fig. 2, compare F, E). For the AP- cells, the negative peak of the response did not exceed the 95th percentile of the shuffled distribution but still showed similar dynamics as in the previous analysis (Fig. 2F). We described response dynamics by fitting a double exponential function (Fig. 2E,F black lines, and see Materials and Methods) and compared the time courses of the normalized inhibitory and excitatory responses. Following air puff stimulations without a run onset, the activation of AP+ cells displayed a much faster time course than the deactivation of the AP- cells (Fig. 2H; FWHM  $262 \pm 30$  ms for AP+ cells versus  $1,183 \pm 60$  ms for AP- cells. Values with 95% confidence intervals after bootstrapping). For the stimuli that triggered locomotion, we found that the decay of the AP+ cell response was indeed longer than in the other scenario while the deactivation of the AP- cells followed a similar time course (Fig. 2I; FWHM  $1,457 \pm 90$  ms for AP+ cells versus  $1,222 \pm 63$  ms for AP- cells. Values with 95% confidence intervals after bootstrapping).

We also compared the response amplitude of AP+ and AP- cells with respect to whether the air puff stimulation triggered locomotion, by fitting a linear mixed effects model to each group of cells, considering the repeated measures of cells and mice-wise contributions. In this test we included only mice that showed behaviorally both types of responses. Using this test design, we did not find a difference in response amplitude for the AP+ cells (Fig. 2J; permutation test on the ranks of cells  $p = 0.52$ ,  $n = 46$ ), nor for the AP- cells (Fig. 2K; permutation test on the ranks of cells  $p = 0.49$ ,  $n = 1,936$ ). An intraclass correlation  $< 0.3$  ( $0.19$  and  $0.004$  for AP+ and AP- cells, respectively) showed that the test result was not driven by individual animals (Extended Data Fig. 2-1F,G).

To control whether running onsets alone would give rise to similar response dynamics or how the observed dynamics could be influenced by the locomotion onset, we analyzed a set of sessions without air puff stimulation recorded from the same animals and used the running onsets as stimulation times (Fig. 2G). Using the same criteria as for the air puff response, we found that across animals  $1.5 \pm 0.4\%$  of active granule cells responded to the running onset, which is lower than that observed to the air puff response ( $2.6\%$ ). However, the dynamics did not show the sharp onset we observed for air puff stimulation. We compared the amplitudes of responsive and nonresponsive granule cells between spontaneous running onsets and post air puff stimulation amplitudes. For responsive cells we found a significant difference between air puff and spontaneous running onsets (Fig. 2L; permutation test on the ranks of cells  $p = 0.001$ ,  $n = 52$ ), where the mean amplitudes of individual cells were higher for the cells that responded to running onsets. We did not find a significant difference for the amplitudes of nonresponding cells (Fig. 2M; permutation test on the ranks of cells  $p = 0.11$ ,  $n = 2,954$ ). Again, an intraclass correlations were  $< 0.3$  ( $0.2$  and  $0.04$  for responsive and nonresponsive granule cells, respectively), which showed that the test result was not driven by individual animals (Extended Data Fig. 2-1H,I). Taken together, the onset of locomotion cannot explain the response dynamics for the AP+ or the AP- cells that we observed but could act as a modulating factor explaining the differences we found between the stimulation with and without triggered locomotion onsets.

### Correlation of MPP input activity with granule cell responses

Next, we asked how sensory information of the air puff stimulation is transmitted to the dentate gyrus. The medial entorhinal cortex (MEC) is one of the major inputs into DG via the medial perforant path (MPP). We therefore expressed the red

←  
air puff. Bottom yellow panel, Mean pupil dynamics. Top blue panel, Z-scored  $\text{Ca}^{2+}$ -event onsets of AP+ cells. Data is averaged over all cells and stimuli and z-scored with respect to baseline. Bottom blue panel, Z-scored  $\text{Ca}^{2+}$  event onsets of AP- cells. Shaded area in all panels denotes SEM and the gray line represents shuffled data with 95th percentiles. Extended Data Figure 2-1 shows the relation between granule cell activation and triggered running initiation for individual animals. **F**, Like **E** for air puff stimuli that triggered running onsets. **G**, Like **E** for spontaneous running onsets. **H**, Normalized time courses for the mean activity of AP+ cells (dark blue line) and of AP- granule cells (light blue line) as fitted from the granule cell activity in **E**. For comparison the sign of the inhibited granule cell activity signals was inverted. Filled area depicts the 95% confidence interval of each fit after bootstrapping. **I**, Same as **H** with data from **F** for air puff stimuli that triggered running onsets. **J**, Swarm chart of response amplitudes of AP+ cells after air puff stimuli that caused running initiation versus air puffs that did not cause running initiation; black lines depict the mean values. Permutation test on the ranks of cells,  $p = 0.52$ ,  $n = 46$  cells. **K**, Same as **J** for AP- cells. Permutation test on the ranks of cells,  $p = 0.49$ ,  $n = 1,936$  cells. **L**, Swarm chart of response amplitudes of AP+ cells after air puff stimulation and for spontaneous running onsets without air puff stimulation; black lines depict the mean values. Permutation test on the ranks of cells,  $p = 0.001$ ,  $n = 52$  cells. **M**, Same as **L** for AP- cells. Permutation test on the ranks of cells,  $p = 0.11$ ,  $n = 2,954$  cells.

shifted  $\text{Ca}^{2+}$  indicator jRGECO1a in MEC excitatory cells using viral gene transfer under the CaMKII promoter in Thy1 GCaMP6 animals. This allowed us to simultaneously monitor the activity of the medial perforant path as well as granule cells, as previously described (Pofahl et al., 2021; see Materials and Methods section; Fig. 3A,B).

Air puff stimulation reliably elicited responses of the MPP in the dentate molecular layer in  $86 \pm 3\%$  of all applied stimuli (Fig. 3C,D,  $n = 3$  mice). In cases where the air puff did not trigger locomotion, a clear peak of MPP bulk fluorescence with a subsequent decay was observed following the stimulus (Fig. 3C). In cases in which mice started running after the stimulus, the initial fluorescence peak was followed by a significantly elevated level of fluorescence (Fig. 3D). This elevation can be explained by the correlation of the MPP input signal to running speed (Pofahl et al., 2021) which we also observed in our control data of spontaneous running onsets (Fig. 3E). Using ROC analysis, we found that the sharp fluorescence peak was a good classifier for the air puff stimulus in every mouse (Fig. 3F).

The simultaneous recording of MPP bulk fluorescence and granule cell signals allowed us to analyze the direct correlation between the MPP input and the responding AP+ granule cells as well as the other AP- granule cells. To use comparable signals for correlation analysis, we used the  $\Delta f/F$  signals of both MPP bulk and granule cell activity while ignoring delays  $>1$  s which would be shaped by the respective  $\text{Ca}^{2+}$  indicator dynamics (Fig. 3G). Since MPP signal and AP+ cells were both correlated to the air puff stimuli, we also found a correlation between these two signals and analogously an anticorrelation between MPP and the mean signal of the AP- cells (Fig. 3H). Looking at the correlation of individual granule cells to the MPP input following the stimulus, we found that 4/5 of AP+ cells were strongly correlated to the MPP and 1/5 cell was weaker, but still positively correlated (Fig. 3I;  $r = 0.6 \pm 0.26$ , mean  $\pm$  SD). The distribution of the other granule cells was centered at  $r = -0.09$  but with long symmetric tails toward positive and negative correlations (SD = 0.35). While the mean  $r$  value close to zero seems to contradict the clear anticorrelation of the average signal (Fig. 3H), this rather highlights that the inhibitory effect is difficult to grasp when looking at individual sparsely active granule cells but becomes evident when looking at the entire ensemble. Comparing the correlation coefficients of AP+ versus AP- cells, we found this difference to be significant ( $n = 5$  vs 263 cells for responder and nonresponders, respectively. Subsampling with size matched groups median  $p = 0.016$ , 80% of  $p$  values  $< 0.05$ , 1,000 iterations).

Next, we asked whether the response amplitudes of granule cells would directly correlate to the variations of the MPP input amplitude following the air puff stimuli. To that end, we subtracted from each signal its mean response and calculated the correlation of the remaining amplitudes analogous to the concept of noise correlation (Averbeck et al., 2006). We did this across all stimuli between the MPP input and each granule cell. For the AP+ granule cells, we found that all noise correlation coefficients were positive but very small and not indicating a noise correlation (Fig. 3J;  $r = 0.08 \pm 0.08$ , mean  $\pm$  SD). For the nonactivated set of granule cells, we found a lower mean value close to zero but again a broad distribution of values ( $r = 0.01 \pm 0.16$ , mean  $\pm$  SD). Hence, in our data given the small number of AP+ cells, we did not find evidence that the response amplitude would directly correlate to the amplitude of the MPP input, which suggests that there are other factors additionally to the MPP input that influence granule cell activity.

### MPP activation mainly induces inhibition in dentate granule cells

The in vivo imaging data imply that sensory stimulation elicits strong and widespread inhibition controlling activity of the granule cell ensemble. Therefore, we next investigated the direct excitatory and inhibitory response of individual granule cells to MPP activation.

To stimulate MPP input selectively, we expressed Chr2-mCherry under the CaMKII promoter in the medial entorhinal cortex using viral gene transfer (Extended Data Fig. 4-2A,B; see Materials and Methods). In hippocampal slices prepared from these mice, light stimulation evoked EPSCs and IPSCs. Combined application of TTX and 4-AP blocked the light-evoked IPSCs, but not EPSCs (Extended Data Fig. 4-2C,D). This demonstrates that under these conditions, MPP stimulation elicits monosynaptic EPSCs, while IPSCs are mediated polysynaptically. To study the properties of MPP-evoked responses of individual granule cells in vivo, we obtained in vivo patch-clamp whole-cell recordings from dorsal hippocampal dentate gyrus granule cells in anesthetized C57BL/6 mice that also expressed Chr2-mCherry under the CaMKII promoter in the medial entorhinal cortex (Fig. 4A;  $n = 9$  cells, 1 cell per animal). MEC principal cell somata were optogenetically stimulated with 473 nm light via an implanted light fiber above MEC. Only cells that showed granule cell morphology through biocytin filling and sufficient Chr2-mCherry MPP expression in post hoc imaging were included in the analysis (example in Fig. 4A).

Optogenetic MPP stimulation elicited a brief low-amplitude depolarization followed by a hyperpolarization of larger amplitude (Fig. 4B). This was true at different membrane potentials when adjusted with constant current injection. Of note, larger amplitude hyperpolarizations were also observed at membrane potentials comparable to those reported previously (Pernía-Andrade and Jonas, 2014).

To isolate excitatory ( $g_e$ ) and inhibitory conductances ( $g_i$ ), we altered the membrane potential of granule cells to four different levels using constant current injections. At each of these potentials, we stimulated perforant path-evoked synaptic potentials with 10 ms pulses of blue light (Fig. 4B). At different current injection magnitudes, synaptic response voltage waveforms are altered because of the difference in membrane potential (Fig. 4C). Using these different waveforms,  $g_e$  and  $g_i$  can be estimated throughout the time course of the postsynaptic potentials (Priebe and Ferster, 2005; see also Materials and Methods). The goodness-of-fit for this model was estimated for every cell which confirmed a good correspondence between data and model result (Extended Data Fig. 4-1). We found that the inhibitory conductance was much



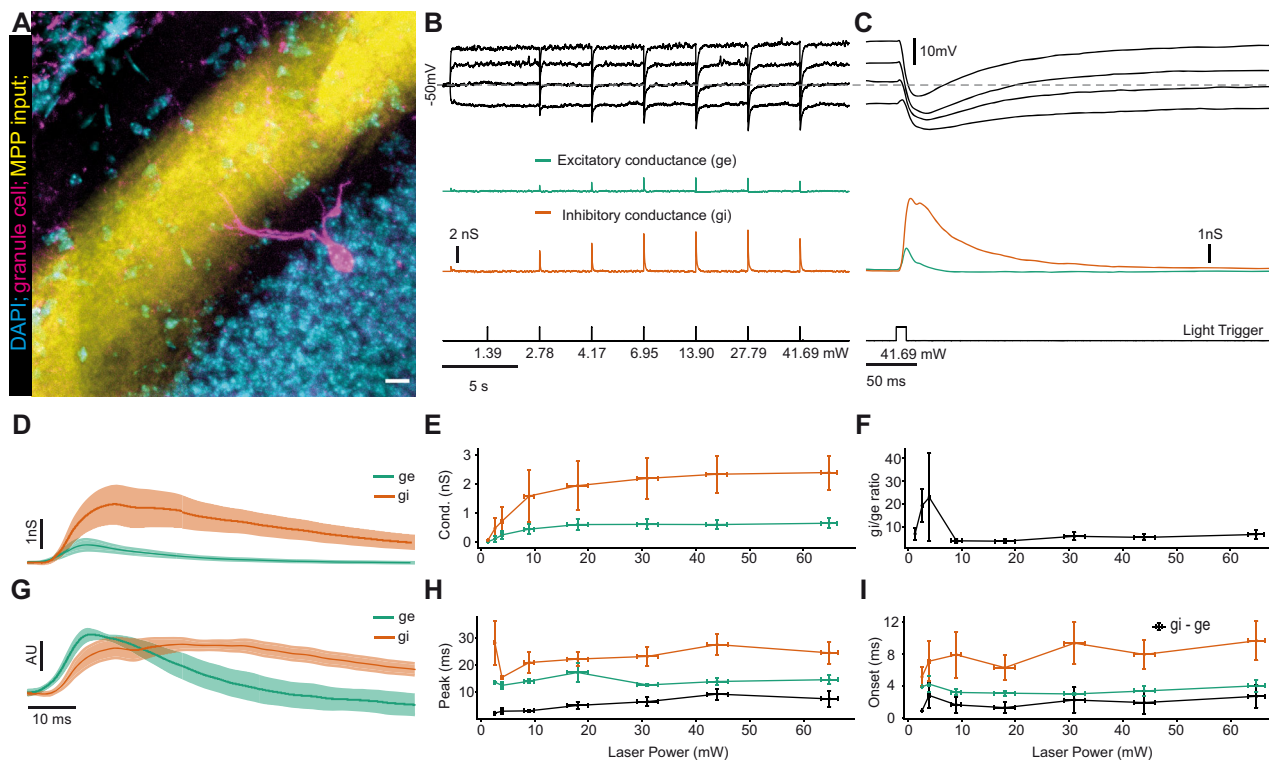


**Figure 4.** In vivo patch-clamp analysis of perforant-path-triggered excitation and inhibition in granule cells. **A**, Post hoc reconstruction of a patched granule cell (magenta) within the hippocampal granule cell layer (DAPI stained cell bodies, cyan) and the ChR2 expressing axons from MPP (yellow). **B**, Top panel (black), EPSP/IPSP voltage responses of the granule cell potential to light stimulation of afferent fibers recorded at four different current injections. Middle panels (green and orange), Estimated excitatory and inhibitory conductances, respectively. Bottom panel, Times and intensities (power at fiber end) of light stimulation. The dashed line depicts the resting membrane potential of  $-50$  mV. **C**, Close-up of the last stimulation shown in **B**. **D**, Average pooled responses  $\pm$  SEM of excitatory and inhibitory conductance (green and orange, respectively) at maximum light stimulation intensity with SEM ( $n = 9$  cells). **E**, Pooled responses measured at different light stimulation intensities.  $x$ -error bars denote estimated variability in laser power at,  $y$ -error bars denote SEM. **F**, Inhibition–excitation ratio calculated from **E** for different stimulation intensities.  $x$ -error bars denote estimated variability in laser power at,  $y$ -error bars denote SEM. **G**, Normalized peak amplitude of conductance responses shown in **D** to illustrate the time course of both conductances in comparison. Excitatory conductance FWHM =  $22 \pm 3$  ms, inhibitory conductance FWHM =  $45 \pm 7$  ms.  $x$ -error bars denote estimated variability in laser power at,  $y$ -error bars denote SEM. **H**, Delay between the stimulation time and the peaks of excitatory and inhibitory conductance (green and orange, respectively) as well as the delay between both peaks (black).  $x$ -error bars denote estimated variability in laser power at,  $y$ -error bars denote SEM. **I**, Delay between the stimulation time of excitatory and inhibitory to conductance response onset as well as the delay between both onsets (black).  $x$ -error bars denote estimated variability in laser power at,  $y$ -error bars denote SEM. Extended Data Figure 4-1 illustrates the goodness of fit estimation for each patched granule cell in the dataset. Extended Data Figure 4-2 illustrates the recruitment of EPSCs and IPSCs in granule cells following optogenetic MPP stimulation in acute slices. Extended Data Figure 4-3 illustrates the conductance responses and resulting E/I balance in response to different stimulation powers in granule cells in acute slices. Extended Data Figure 4-4 gives a summary of published granule cell E/I ratios in the literature.

larger than the excitatory conductance for all cells (Fig. 4D, data shown for maximal laser power). This was true over a range of stimulation intensities (Fig. 4E,F, asterisks indicate one-sample  $t$  tests against 1,  $g_i/g_e$  ratio at maximum stimulation power  $6.7 \pm 2.1$ ).

Aside from the peak magnitude of conductance changes, the relative time course of  $g_e$  and  $g_i$  strongly determines the likelihood and timing of action potential generation in granule cells. The peak normalized averaged waveforms at the highest laser power showed a short onset delay of roughly 2 ms (Fig. 4G). Quantifying the time lag between  $g_e$  and  $g_i$  peak revealed a lag of  $7.5 \pm 3.2$  ms (Fig. 4H) at the highest laser power and an onset delay of  $2.7 \pm 1.5$  ms (Fig. 4I). These short time delays are consistent with the expected strong contribution of feedforward inhibition. Comparing the time courses of the inhibitory and the excitatory conductances, we found that  $g_e$  had a  $\text{FWHM}_e = 22 \pm 3$  ms, which was much shorter than the one of  $g_i$  with  $\text{FWHM}_i = 45 \pm 7$  ms. This suggested a longer lasting inhibitory response compared with the excitatory response.

Taken together, we conclude that MEC stimulation evokes strong, long-lasting inhibition with a short, millisecond scale delay after excitation onset.

### Excitation–inhibition balance across different stimulation frequencies

To test the frequency dependence of the excitation–inhibition (I/E) balance, we studied repetitive stimulation protocols. Theta-band stimulation (5 Hz) responses led to stable excitatory responses over 10 stimulations (Friedman test,  $\chi^2 = 4.61$ ,

$p=0.87$ ), while inhibitory responses decreased (Friedman test,  $\chi^2=21.75$ ,  $p=0.0097$ , Fig. 5A,C,E). Faster stimulation (20 Hz) led to a depression in both excitation and inhibition (Friedman test, excitation:  $\chi^2=55.45$ ,  $p=1.98 \times 10^{-5}$ , inhibition:  $\chi^2=34.89$ ,  $p=0.014$ , respectively; Fig. 5B,D,F). When we computed the ratio of  $g_i$  to  $g_e$ , however, the different dynamics of the two conductances were not sufficient to cause significant differences (Fig. 5G,H; Friedman test, 5 Hz:  $\chi^2=8.03$ ,  $p=0.53$ , 20 Hz:  $\chi^2=25.01$ ,  $p=0.16$ ). We conclude that there are reductions in  $g_i$  during repetitive stimulation that may lead to subtle changes in I/E balance. The latter finding was not statistically significant; however, we note that the statistical power of our analysis was low (0.082 for 5 Hz and 0.33 for 20 Hz).

### Comparison to in vitro analysis of MPP-evoked inhibition

In parallel to the in vivo patch-clamp recordings, we also examined recruitment of granule cells by selective optogenetic MPP activation in the slice preparation (Extended Data Fig. 4-2A,B). Inhibitory and excitatory currents were measured in

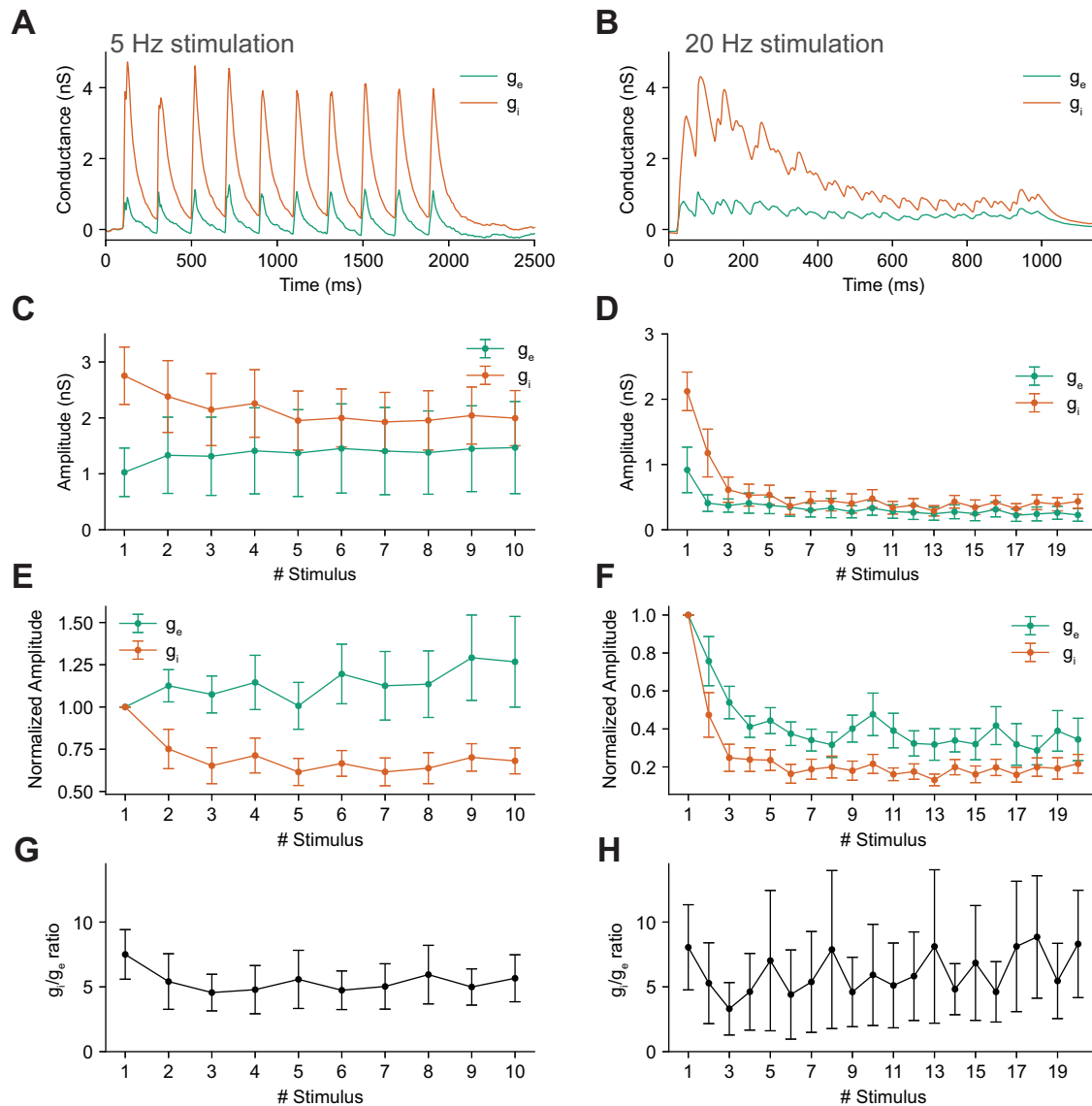


**Figure 5.** Excitation–inhibition balance in granule cells during repetitive stimulation of perforant path in vivo. **A, B**, Representative excitatory and inhibitory conductance traces during 5 and 20 Hz stimulation, respectively. **C**, At 5 Hz excitatory conductance is slightly facilitating while inhibitory conductance is depressing. Error bars denote SEM. Friedman test:  $n=9$ ,  $df=9$ ,  $g_e$ :  $\chi^2=5$ ,  $p=0.87$ ;  $g_i$ :  $\chi^2=22$ ,  $p<0.01$ . **D**, At 20 Hz both excitatory and inhibitory conductance are strongly depressing. Error bars denote SEM. Friedman test:  $n=7$ ,  $df=19$ ,  $g_e$ :  $\chi^2=55$ ,  $p<0.0001$ ;  $g_i$ :  $\chi^2=40$ ,  $p<0.0001$ . **E**, Like **C** with amplitudes normalized to first elicited conductance. Error bars denote SEM.  $n=9$  cells. **F**, Like **D** with amplitudes normalized to first elicited conductance. Error bars denote SEM.  $n=7$  cells. **G**, At 5 Hz inhibitory peak conductance is consistently larger than excitatory during the entire stimulus train. Error bars denote SEM. Friedman test did not show a significant effect of stimulus:  $\chi^2=8.03$ ,  $n=9$ ,  $df=9$ ,  $p=0.53$ . **H**, At 20 Hz the inhibitory peak conductance is also consistently larger than the excitatory during the stimulus train. Error bars denote SEM. Friedman test did not show a significant main effect for stimulus:  $\chi^2=25.01$ ,  $n=7$ ,  $df=19$ ;  $p=0.16$ . Extended Data Figure 5-1 illustrates the E/I balance in responses to frequency stimulation in granule cells in acute slices.

voltage-clamp mode and pharmacologically isolated (Extended Data Fig. 4-2C,D,E; see Materials and Methods). Of note, while stimulation of MPP fibers was carried out optogenetically both in vivo and in vitro, the pharmacological isolation could only be carried out in the in vitro condition.

For optogenetic stimulation in the slice, the light stimulation was focused on the terminal region in the medial molecular layer of the dentate gyrus. The optogenetically evoked responses saturated at light powers comparable to the in vivo experiments (Extended Data Fig. 4-2F). The respective inhibitory and excitatory conductances were calculated using the reversal potentials (Extended Data Fig. 4-3A,B). The kinetics were generally comparable to the in vivo experiments, with similar onset times of the inhibitory and excitatory conductances (Extended Data Fig. 4-3C; excitatory conductance onset time:  $F_{(1,16)} = -1.91, p = 0.07$ , inhibitory conductance onset time:  $F_{(1,19)} = -1.55, p = 0.14$ ). The same was true for the time to peak of the inhibitory conductance, while the rise for the excitatory conductance was faster in vitro (Extended Data Fig. 4-3D; excitatory conductance time to peak:  $F_{(1,16)} = -6.39, p < 0.01$ , inhibitory conductance onset time:  $F_{(1,19)} = -1.71, p = 0.10$ ). A difference was apparent when computing the I/E ratio, which was more than an order of magnitude lower than that found in our in vivo granule cell recordings (Extended Data Fig. 4-3E, Fig. 4F;  $< 0.5$  in vitro vs 7.50 to 5.66 in vivo,  $F_{(1,19)} = -3.2, p < 0.1$ ).

We further examined the dynamics of inhibitory and excitatory responses, as well as I/E ratios during repetitive stimulation in vitro. In the in vitro condition, both  $g_i$  and  $g_e$  were reduced significantly during stimulation trains of any frequency (5–50 Hz; Extended Data Fig. 5-1A–C; Friedman test, statistics for all frequencies see figure legend Extended Data Fig. 5-1). Comparable to in vivo recordings, the I/E balance was maintained in in vitro recordings during stimulation trains at both 5 and 10 Hz (Friedman test, n.s.; Extended Data Fig. 5-1D). At higher stimulation frequencies, however, the I/E ratio was significantly increased (Friedman test 20 Hz:  $\chi^2 = 36.98, p = 0.00003$ ; 30 Hz:  $\chi^2 = 31.48, p = 0.0002$ ; Extended Data Fig. 5-1D; statistics for all frequencies see figure legend Extended Data Fig. 5-1).

## Discussion

We show that mild aversive air puff stimulation during immobility triggers an activity cascade through the medial perforant path to the dentate gyrus. While this stimulation leads to a significant direct excitation of a small subset of granule cells (2.6% of recorded cells), the effect on the other granule cells is a 1-s-long lasting inhibition of activity. Further, we show that direct optogenetic stimulation of medial entorhinal cortex cells leads to a fourfold stronger inhibition than excitation in individually patched granule cells in anesthetized mice. This strongly biased E/I balance is also stable for stimulation different frequencies in vivo. Taken together, our findings shed light on the inhibitory effects acting on dentate gyrus granule cells which are necessary to maintain sparse activity levels which are thought to be the basis of pattern separation (Cayco-Gajic and Silver, 2019).

Across brain regions and species, inhibitory circuits shape neuronal population activity. In the hippocampal dentate gyrus, inhibition promotes sparse granule cell activity, which in turn contributes to the function of pattern separation. Numerous studies have examined the circuit properties of inhibition in the dentate gyrus in hippocampal slices, leading to a refined model of the circuit basis of inhibition (Strüber et al., 2015, 2017; Espinoza et al., 2018; Braganza et al., 2020; Guzman et al., 2021).

However, there is substantial intrahippocampal connectivity within the dentate gyrus that exceeds the dimensions of a typical slice preparation (Buckmaster and Schwartzkroin, 1995; Sik et al., 1997; Bienkowski et al., 2018; Yen et al., 2022). Thus, the properties of inhibition recruited in vivo may be different from those predicted by local inhibitory circuits. For this reason, assessing inhibition of the dentate gyrus in in vivo experiments is important and relevant. We have used both in vivo imaging and in vivo patch-clamp recordings to assess the properties of inhibition in the dentate gyrus on the population and single-neuron level. Our data show that medial perforant path stimulation selectively activates a sparse set of granule cells while simultaneously causing widespread inhibition across the remainder of the granule cell population. In addition, we show with in vivo whole-cell recordings that medial perforant path-triggered inhibition is large, fast, and maintained during repetitive stimulation.

Our two-photon in vivo imaging data show that on average only 2.6% of dentate gyrus granule cells respond significantly to sensory-evoked MPP activation. Because even this responding subclass of granule cells responds unreliably to air puff stimulation, this means that the fraction of responding cells activated after a given air puff is very low. Nevertheless, the remaining granule cells were on average suppressed over a time window of up to one second. This is generally consistent with the sparse firing of granule cells observed with both imaging and in vivo electrophysiology (Danielson et al., 2016; Diamantaki et al., 2016; Pilz et al., 2016; GoodSmith et al., 2017; Senzai and Buzsáki, 2017; Hainmueller and Bartos, 2018; van Dijk and Fenton, 2018). A similar phenomenon has also been observed for cue-responsive DG populations, which—when activated—also lead to significant inhibition of spontaneous and place-related firing of the remaining granule cell population (Tuncdemir et al., 2022). The strong contrast in granule cell responses with sparse activation and widespread inhibition is in line with a “k-winners take it all” model that has been proposed for the DG network (O’Reilly and McClelland, 1994; de Almeida et al., 2009; Braganza et al., 2020).

Our design aimed at investigating sensory-related responses without additional behavioral confounds. We therefore limited our stimulation time points to resting periods, to exclude space and speed as confounding factors. We also randomized stimulation in time and space to prevent temporal or spatial learning. Still, we observed differences in granule

responses depending on whether locomotion was initiated by the air puff stimulation or not. The response amplitudes were no significantly different in either scenario or for the AP+ or the AP- cells. The dynamics of the response without running initiation were fast with a FWHM  $262 \pm 30$  ms for the AP+ cells, while they were much slower for the same cell population with running onsets. We cannot conclusively dissect how much of the late excitation is caused by the air puff versus running. However, it is likely that the late excitation is due to locomotion, because similar prolonged excitation was observed in pure running onsets without air puff stimulation both in the granule cells and the MPP bulk signal.

The simultaneous recordings of air puff responses in MPP bulk input and individual granule cell activity illustrate the general correlation in this feed forward network. One feature hypothesized for the dentate gyrus is the orthogonalization of its inputs which underlies the concept of pattern separation (Cayco-Gajic and Silver, 2019). While our data showed the direct correlation of MPP input to the overall response in the granule cells, we did not observe a correlation of response amplitude to the variations of the input amplitude. This suggests that for the AP+ cells that we measured, the individual stimulus-wise response amplitude could also be influenced by other inputs or modulatory factors. Given the small number of AP+ cells in our paired recordings, this conclusion must be interpreted with caution, and we cannot exclude that correlations might become apparent with more cells. However, the lack of correlation is in line with the general observed unreliability of granule cell responses with no granule cell responding to more than two-thirds of stimuli and 18% of all granule cells responding exactly once. Taken together, these data could shed light on how the dentate granule cell network generates unique output patterns from one of its input sources.

While the *in vivo* imaging experiments serve only as an indirect measure of the inhibitory effects onto granule cells, our whole-cell recordings of granule cells directly show the strong inhibitory conductance change triggered by MPP activation. There were several remarkable features of DG inhibition. Firstly, inhibition was large, with high inhibition–excitation ratios. This is consistent with prior work describing prominent IPSPs in granule cells following MPP activation (Buckmaster and Schwartzkroin, 1995), although this study did not determine inhibition–excitation ratios quantitatively. *In vitro*, on the other hand, we found excitation to be larger than inhibition. We note that this is in contrast to previous slice work. Ewell and Jones (2010) found IPSCs to be approximately three times larger than EPSCs and Marín-Burgin et al. (2012) find them to be approximately twice as large (see summary of published work in Extended Data Fig. 4-4). We surmise that this could be due to methodological differences. Firstly, we have isolated excitatory and inhibitory PSCs with gabazine in every individual experiment, while previous studies relied on voltage clamping to the respective reversal potentials. Secondly, we stimulated MPP using optogenetic approaches in both our *in vivo* and *in vitro* recordings, while previous *in vitro* studies employed electrical stimulation. Although some studies used AMPAR blockers (Ewell and Jones, 2010) to exclude direct stimulation of GABAergic axons, this was not done in all studies and experiments. Direct stimulation of GABAergic axons would be expected to enhance the measured inhibition. Other factors also affect I/E balance, for instance, if recordings were done from dorsal or ventral hippocampus or recording temperature. The latter is directly addressed in one paper (Hsu et al., 2016), which clearly shows much smaller I/E ratios at body temperature similar to the *in vivo* condition (0.4 at 34° vs ~2 at 23°C; see Extended Data Fig. 4-4). However, even given the diverse values of I/E balance reported under different conditions *in vitro*, the I/E ratio we measured *in vivo* is still roughly twice as large as the largest ratio measured *in vitro*.

We also examined the dynamic features of inhibition–excitation ratios. We found that *in vitro*, stimulation frequencies ranging from 5 to 50 Hz caused frequency-dependent decreases of both inhibition and excitation. At frequencies >10 Hz, excitatory responses showed larger decreases than inhibition, leading to dynamic increases in I/E ratios. These *in vitro* findings are in line with published work (Marín-Burgin et al. (2012), their Fig. S8; Pardi et al. (2015), their Fig. 3 Supplement 2; but see Hsu et al., 2016]. In our *in vivo* experiments, inhibitory responses were significantly depressed at 5 and 20 Hz, whereas excitatory responses showed significant depression only at 20 Hz. Despite these differential changes, I/E ratios were not significantly altered during repetitive stimulation at any frequency. We note that the statistical power of these analyses of I/E ratios was low, and larger sample sizes could reveal reductions of I/E balance during repetitive stimulation. Nonetheless, the fact that *in vivo* I/E balance is either unchanged or potentially reduced under some conditions appears different from our and previous *in vitro* studies (Marín-Burgin et al., 2012; Pardi et al., 2015) showing increased I/E ratios during stimulation trains.

Decreased I/E ratios due to stronger adaptation of inhibition compared with excitation have been observed in sensory cortex and has been proposed to act as a gain mechanism active during sustained sensory activity (Heiss et al., 2008; Cohen-Kashi Malina et al., 2013). In the dentate gyrus, previous studies have proposed that this region has frequency-dependent filtering properties (Hsu, 2007; Ewell and Jones, 2010; Marín-Burgin et al., 2012; Scullin and Partridge, 2012; Pardi et al., 2015; Lee et al., 2016). Specifically, measurements of pre- and postsynaptic activity suggest that the dentate gyrus may act as a low-pass filter (Scullin and Partridge, 2012), consistent with our observation of reduced inhibition but not excitation during low-frequency 5 Hz activation. At higher (20 Hz) stimulation frequencies, both inhibition and excitation are reduced. This frequency range is relevant to cognition, as novelty experience and certain types of exploratory activity are associated with increased activity in the gamma or beta frequency bands (Rangel et al., 2016; Trimper et al., 2017; Barth et al., 2018). Moreover, gamma frequency-related communication between the entorhinal cortex and dentate gyrus support specific types of memory synchronization (Fernández-Ruiz et al., 2021). Finally, pattern separation has been proposed to operate particularly efficiently at gamma frequencies, due to frequency-dependent properties of inhibitory feedback circuits (Braganza et al., 2020).

Finally, we show that inhibition in DG is fast, lagging excitation by only 5–10 ms on average. While we cannot dissect contributions of feedforward and feedback inhibition rigorously, it is likely that there is a strong contribution of feedforward inhibition to initial phases of MPP-induced inhibition. Indeed, activation of some types of interneurons in the dentate gyrus can even precede the activation of granule neurons (Li et al., 2013).

We note that the inhibition assessed by direct patch-clamp recordings was in the order of hundreds of milliseconds, while the inhibition of neuronal activity seen in *in vivo* imaging experiments lasts up to a second. Slow IPSPs in granule cells have been described (de Koninck and Mody, 1997; Mircheva et al., 2019). Because our *in vivo* recordings required the intracellular presence of QX314, which blocks GABA<sub>B</sub>-activated K<sup>+</sup> channels (Nathan et al., 1990; Andrade, 1991), it is possible that our patch-clamp recordings underestimate the duration of synaptically evoked inhibition after MPP activation. Further, the lasting activation of some granule cells that we have seen in our data could also lead to a further recruitment of feedback inhibition, which could lead to the long-lasting inhibition of the nonresponding granule cells.

In summary, we show that MPP input evokes fast and strong inhibition that causes widespread depression of granule cell population activity. This may be relevant for pattern separation, a key proposed function of the dentate gyrus.

## References

- Andrade R (1991) Blockade of neurotransmitter-activated K<sup>+</sup> conductance by QX-314 in the rat hippocampus. *Eur J Pharmacol* 199:259–262.
- Ang CW, Carlson GC, Coulter DA (2006) Massive and specific dysregulation of direct cortical input to the hippocampus in temporal lobe epilepsy. *J Neurosci* 26:11850–11856.
- Averbeck BB, Latham PE, Pouget A (2006) Neural correlations, population coding and computation. *Nat Rev Neurosci* 7:358–366.
- Barth AM, Domonkos A, Fernandez-Ruiz A, Freund TF, Varga V (2018) Hippocampal network dynamics during rearing episodes. *Cell Rep* 23:1706–1715.
- Barth AM, Jelitai M, Vasarhelyi-Nagy MF, Varga V (2023) Aversive stimulus-tuned responses in the CA1 of the dorsal hippocampus. *Nat Commun* 14:6841.
- Bartos M, Vida I, Frotscher M, Geiger JR, Jonas P (2001) Rapid signaling at inhibitory synapses in a dentate gyrus interneuron network. *J Neurosci* 21:2687–2698.
- Berron D, Schütze H, Maass A, Cardenas-Blanco A, Kujif HJ, Kumaran D, Düzel E (2016) Strong evidence for pattern separation in human dentate gyrus. *J Neurosci* 36:7569–7579.
- Bienkowski MS, et al. (2018) Integration of gene expression and brain-wide connectivity reveals the multiscale organization of mouse hippocampal networks. *Nat Neurosci* 21:1628–1643.
- Braganza O, Mueller-Komorowska D, Kelly T, Beck H (2020) Quantitative properties of a feedback circuit predict frequency-dependent pattern separation. *Elife* 9:e53148.
- Buckmaster PS, Schwartzkroin PA (1995) Interneurons and inhibition in the dentate gyrus of the rat *in vivo*. *J Neurosci* 15:774–789.
- Cayco-Gajic NA, Silver RA (2019) Re-evaluating circuit mechanisms underlying pattern separation. *Neuron* 101:584–602.
- Cohen-Kashi Malina K, Jubran M, Katz Y, Lampl I (2013) Imbalance between excitation and inhibition in the somatosensory cortex produces postadaptation facilitation. *J Neurosci* 33:8463–8471.
- Cohen-Kashi Malina K, Mohar B, Rappaport AN, Lampl I (2016) Local and thalamic origins of correlated ongoing and sensory-evoked cortical activities. *Nat Commun* 7:12740.
- Dana H, Chen TW, Hu A, Shields BC, Guo C, Looger LL, Kim DS, Svoboda K (2014) Thy1-GCaMP6 transgenic mice for neuronal population imaging *in vivo*. *PLoS One* 9:e108697.
- Dana H, et al. (2016) Sensitive red protein calcium indicators for imaging neural activity. *Elife* 5:e12727.
- Danielson NB, et al. (2016) Distinct contribution of adult-born hippocampal granule cells to context encoding. *Neuron* 90:101–112.
- de Almeida L, Idiart M, Lisman JE (2009) A second function of gamma frequency oscillations: an E%-max winner-take-all mechanism selects which cells fire. *J Neurosci* 29:7497–7503.
- de Koninck Y, Mody I (1997) Endogenous GABA activates small-conductance K<sup>+</sup> channels underlying slow IPSCs in rat hippocampal neurons. *J Neurophysiol* 77:2202–2208.
- Diamantaki M, Frey M, Berens P, Preston-Ferrer P, Burgalossi A (2016) Sparse activity of identified dentate granule cells during spatial exploration. *Elife* 5.
- Espinoza C, Guzman SJ, Zhang X, Jonas P (2018) Parvalbumin+ interneurons obey unique connectivity rules and establish a powerful lateral-inhibition microcircuit in dentate gyrus. *Nat Commun* 9:4605.
- Ewell LA, Jones MV (2010) Frequency-tuned distribution of inhibition in the dentate gyrus. *J Neurosci* 30:12597–12607.
- Fernández-Ruiz A, Oliva A, Soula M, Rocha-Almeida F, Nagy GA, Martín-Vázquez G, Buzsáki G (2021) Gamma rhythm communication between entorhinal cortex and dentate gyrus neuronal assemblies. *Science* 372:eabf3119.
- GoodSmith D, Chen X, Wang C, Kim SH, Song H, Burgalossi A, Christian KM, Knierim JJ (2017) Spatial representations of granule cells and mossy cells of the dentate gyrus. *Neuron* 93:677–690.e5.
- Greenberg DS, Kerr JND (2009) Automated correction of fast motion artifacts for two-photon imaging of awake animals. *J Neurosci Methods* 176:1–15.
- Guzman SJ, Schlögl A, Espinoza C, Zhang X, Suter BA, Jonas P (2021) How connectivity rules and synaptic properties shape the efficacy of pattern separation in the entorhinal cortex-dentate gyrus-CA3 network. *Nat Comput Sci* 1:830–842.
- Hainmueller T, Bartos M (2018) Parallel emergence of stable and dynamic memory engrams in the hippocampus. *Nature* 558:292–296.
- Hainmueller T, Cazala A, Huang L-W, Bartos M (2024) Subfield-specific interneuron circuits govern the hippocampal response to novelty in male mice. *Nat Commun* 15:714.
- Heiss JE, Katz Y, Ganmor E, Lampl I (2008) Shift in the balance between excitation and inhibition during sensory adaptation of S1 neurons. *J Neurosci* 28:13320–13330.
- Hsu D (2007) The dentate gyrus as a filter or gate: a look back and a look ahead. *Prog Brain Res* 163:601–613.
- Hsu T-T, Lee C-T, Tai M-H, Lien C-C (2016) Differential recruitment of dentate gyrus interneuron types by commissural versus perforant pathways. *Cereb Cortex* 26:2715–2727.
- Leal SL, Yassa MA (2018) Integrating new findings and examining clinical applications of pattern separation. *Nat Neurosci* 21:163–173.
- Lee C-T, Kao M-H, Hou W-H, Wei Y-T, Chen C-L, Lien C-C (2016) Causal evidence for the role of specific GABAergic interneuron types in entorhinal recruitment of dentate granule cells. *Sci Rep* 6:36885.
- Leutgeb JK, Leutgeb S, Moser MB, Moser EI (2007) Pattern separation in the dentate gyrus and CA3 of the hippocampus. *Science* 315:961–966.
- Li Y, Stam FJ, Aimone JB, Goulding M, Callaway EM, Gage FH (2013) Molecular layer perforant path-associated cells contribute to feedforward inhibition in the adult dentate gyrus. *Proc Natl Acad Sci U S A* 110:9106–9111.
- Liu D, et al. (2025) A hypothalamic circuit underlying the dynamic control of social homeostasis. *Nature* 640:1000–1010.

- Madar AD, Ewell LA, Jones MV (2019) Pattern separation of spiketrains in hippocampal neurons. *Sci Rep* 9:5282.
- Marín-Burgin A, Mongiat LA, Pardi MB, Schinder AF (2012) Unique processing during a period of high excitation/inhibition balance in adult-born neurons. *Science* 335:1238–1242.
- Mircheva Y, Peralta MR, Tóth K (2019) Interplay of entorhinal input and local inhibitory network in the hippocampus at the origin of slow inhibition in granule cells. *J Neurosci* 39:6399–6413.
- Nathan T, Jensen MS, Lambert JDC (1990) The slow inhibitory post-synaptic potential in rat hippocampal CA1 neurones is blocked by intracellular injection of QX-314. *Neurosci Lett* 110:309–313.
- Okun M, Lampl I (2008) Instantaneous correlation of excitation and inhibition during ongoing and sensory-evoked activities. *Nat Neurosci* 11:535–537.
- O'Reilly RC, McClelland JL (1994) Hippocampal conjunctive encoding, storage, and recall. Avoiding a trade-off. *Hippocampus* 4:661–682.
- Pardi MB, Ogando MB, Schinder AF, Marin-Burgin A (2015) Differential inhibition onto developing and mature granule cells generates high-frequency filters with variable gain. *Elife* 4:e08764.
- Pernía-Andrade AJ, Jonas P (2014) Theta-gamma-modulated synaptic currents in hippocampal granule cells in vivo define a mechanism for network oscillations. *Neuron* 81:140–152.
- Pilz GA, Carta S, Stauble A, Ayaz A, Jessberger S, Helmchen F (2016) Functional imaging of dentate granule cells in the adult mouse hippocampus. *J Neurosci* 36:7407–7414.
- Pnevmatikakis EA, et al. (2016) Simultaneous denoising, deconvolution, and demixing of calcium imaging data. *Neuron* 89:285–299.
- Pofahl M, et al. (2021) Synchronous activity patterns in the dentate gyrus during immobility. *Elife* 10:e65786.
- Priebe NJ, Ferster D (2005) Direction selectivity of excitation and inhibition in simple cells of the cat primary visual cortex. *Neuron* 45:133–145.
- Rangel LM, Rueckemann JW, Riviere PD, Keefe KR, Porter BS, Heimbuch IS, Budlong CH, Eichenbaum H (2016) Rhythmic coordination of hippocampal neurons during associative memory processing. *Elife* 5:e09849.
- Reimer J, Froudarakis E, Cadwell CR, Yatsenko D, Denfield GH, Tolias AS (2014) Pupil fluctuations track fast switching of cortical states during quiet wakefulness. *Neuron* 84:355–362.
- Sakon JJ, Suzuki WA (2019) A neural signature of pattern separation in the monkey hippocampus. *Proc Natl Acad Sci U S A* 116:9634–9643.
- Scullin CS, Partridge LD (2012) Modulation by pregnenolone sulfate of filtering properties in the hippocampal trisynaptic circuit. *Hippocampus* 22:2184–2198.
- Senzai Y, Buzsáki G (2017) Physiological properties and behavioral correlates of hippocampal granule cells and mossy cells. *Neuron* 93:691–704.e5.
- Sik A, Penttonen M, Buzsáki G (1997) Interneurons in the hippocampal dentate gyrus. An in vivo intracellular study. *Eur J Neurosci* 9:573–588.
- Stefanelli T, Bertolini C, Lüscher C, Müller D, Mendez P (2016) Hippocampal somatostatin interneurons control the size of neuronal memory ensembles. *Neuron* 89:1074–1085.
- Steinmetz NA, et al. (2017) Aberrant cortical activity in multiple GCaMP6-expressing transgenic mouse lines. *eNeuro* 4:ENEURO.0207-17.2017.
- Strüber M, Jonas P, Bartos M (2015) Strength and duration of perisomatic GABAergic inhibition depend on distance between synaptically connected cells. *Proc Natl Acad Sci U S A* 112:1220–1225.
- Strüber M, Sauer J-F, Jonas P, Bartos M (2017) Distance-dependent inhibition facilitates focality of gamma oscillations in the dentate gyrus. *Nat Commun* 8:758.
- Szabo GG, Du X, Oijala M, Varga C, Parent JM, Soltesz I (2017) Extended interneuronal network of the dentate gyrus. *Cell Rep* 20:1262–1268.
- Trimper JB, Galloway CR, Jones AC, Mandi K, Manns JR (2017) Gamma oscillations in rat hippocampal subregions dentate gyrus, CA3, CA1, and subiculum underlie associative memory encoding. *Cell Rep* 21:2419–2432.
- Tuncdemir SN, Grosmark AD, Turi GF, Shank A, Bowler JC, Ordek G, Losonczy A, Hen R, Lacefield CO (2022) Parallel processing of sensory cue and spatial information in the dentate gyrus. *Cell Rep* 38:110257.
- van Dijk MT, Fenton AA (2018) On how the dentate gyrus contributes to memory discrimination. *Neuron* 98:832–845.e5.
- Yen T-Y, Huang X, MacLaren DAA, Schlesiger MI, Monyer H, Lien C-C (2022) Inhibitory projections connecting the dentate gyri in the two hemispheres support spatial and contextual memory. *Cell Rep* 39:110831.
- Yuan M, Cazala A, Goedeke S, Leibold C, Sauer J-F, Bartos M (2025) Predictive goal coding by dentate gyrus somatostatin-expressing interneurons in male mice. *Nat Commun* 16:5382.